*Int. J. Electrochem. Sci.*, 15 **(2020)** 5031 – 5041, doi: 10.20964/2020.06.03

**International Journal of**
**ELECTROCHEMICAL**
**SCIENCE**
www.electrochemsci.org

# Superior Cycle Stability of Single Crystal Nickel-Rich Layered Oxides with Micron-Scale Grain Size as Cathode Material for Lithium Ion Batteries

*Cheng Yang*[1,2,*] *Zhenhua Zhu*[3], *Weifeng Wei*[2], *Liangjun Zhou*[2,*]

[1] School of Metallurgy and Environment, Central South University, Changsha 410083, P.R. China
[2] State Key Laboratory of Powder Metallurgy, Central South University, Changsha, Hunan, 410083, P. R. China
[3] School of Chemistry, South China Normal University, Guangzhou,510006, PR China.
[*]E-mail: alexander-zhou@csu.edu.cn, yangchengcsu@163.com

*Received:* 2 February 2020 / *Accepted:* 17 March 2020 / *Published:* 10 May 2020

Ni-rich layered transition metal (TM) oxides are being aggressively developed, due to their high volumetric energy density. However, the severe capacity fading hinders their practical applications such as electric vehicles. As reported, grain boundary of primary particles is expected to play an important role in the performance degradation. Here, single crystal $LiNi_{0.8}Mn_{0.1}Co_{0.1}O_2$ (NCM, S811) with a grain size of 1–4 μm was synthesized by controlling the Li/TM ratio and two-step calcination. Compared with the common agglomerated NCM811 (A811), S811 exhibited the similar initial specific capacity of 198.9 mAh /g at 0.1 C, but much higher capacity retention (96.2% after150 cycles). Further investigations, including morphology analysis, electrochemical tests and observation of internal variation, were carried out to further understand the superiority of S811. The superior performance could be attributed to the better structure stability of single crystal with larger size, which could introduce more $Ni^{2+}$ in the outer layer for inhibiting the phase transformation (H2→H3) and side reactions on the interfaces. This work may provide a promising strategy for long-term cycling stability of nickel-rich NCM-type lithium ion battery.

**Keyword**: nickle-rich layered oxides, micron-scale, single crystal, phase transformation, lithium ion batteries.

## 1. INTRODUCTION

Now that Lithium-ion batteries (LIBs) have been the most successful electrochemical energy source for electronic devices. However, electric device technology advance requires high energy density.[1-4] In order to overcome the range anxiety of LIBs, Ni-rich $Li[Ni_xCo_yMn_{1-x-y}]O_2$ (NCM) has been regarded as a promising option for cathode materials.[5-8] Among a wide range of transition metal (TM) elemental components in NCM, $LiNi_{0.8}Co_{0.1}Mn_{0.1}O_2$ has been gained more and more attentions due to the higher capacity and relatively lower cost.[9,10] However, with the increase of Ni content, traditionally used agglomerated $LiNi_{0.8}Co_{0.1}Mn_{0.1}O_2$ suffers from severer capacity fading. The rapid degradation of Li storage is typically ascribed to surface related chemical degradations and structural instability, which are arising from oxygen release and numerous microcracks. [11-13] Up to now, many strategies have been carried out, including metal substitution, surface modification and gradient composition. Moreover, it is reported that single crystal structure is helpful for electrochemistry performance of cathode materials.[14] Kim et al. proposed significantly enhanced electrochemical performance of fully-developed single crystal $LiNi_{1/3}Co_{1/3}Mn_{1/3}O_2$ and further implied that such crystallization process facilitated the formation of well-defined layered crystal structure.[15] Wu et al. [16] and Dahn et al. [17] both demonstrated the effects of single crystal grain on Ni-rich cathode materials.

Inspired by these above reports, in this work, micron-scale single crystal $LiNi_{0.8}Mn_{0.1}Co_{0.1}O_2$ (S811) with superior cycling stability was designed and controllably synthesized by the adjustment of Li/TM ratio and two-step calcination calcinating at high temperature. Furthermore, the superior electrochemical performances of S811 and A811 are investigated. Owing to the fully-grown crystal grain and reduced content of $Ni^{3+}$, H2→H3 phase transition reaction can be compressed, hence the cracks in primary particles and element dissolution are limited.

## 2. EXPERIMENTAL

### *2.1. Materials Preparation synthesis*

$Ni_{0.8}Co_{0.1}Mn_{0.1}(OH)_2$ were synthesized via a hydroxide coprecipitation method. The typical process of $Ni_{0.8}Co_{0.1}Mn_{0.1}(OH)_2$ preparation was described elsewhere.[18,19] The $Ni_{0.8}Co_{0.1}Mn_{0.1}(OH)_2$ precursor was thoroughly mixed with a stoichiometric amount of $LiOH{\cdot}H_2O$ by high-speed ball milling. Firstly, a Li/TM ratio of 0.98 was employed for the mixture $Ni_{0.8}Co_{0.1}Mn_{0.1}(OH)_2$ and $LiOH{\cdot}H_2O$. The mixed powders were preheated in oxygen in an elevator furnace, and the heating rate of 5 °C/min was used to raise the temperature to 870 °C for 6 h. The heated powders were taken out and ground by a grind machine after it is cooled to room temperature. Secondly, additional $LiOH{\cdot}H_2O$ was added to obtain an overall Li/TM ratio of 1.08. The added $LiOH{\cdot}H_2O$ was thoroughly mixed with the product of the first heating using a high-speed ball milling, and then heated in oxygen in the tube furnace at 830 °C for 12 h. The prepared $LiNi_{0.8}Co_{0.1}Mn_{0.1}O_2$ was noted as S811. For comparison, an agglomerated-type sample, noted as A811, was prepared through a traditional approach.[20]

### *2.2. Electrochemical Testing*

During the process of working electrodes fabrication, a slurry of the active cathode materials, polyvinylidene fluoride and conductive agent (SP 1.5%+KS-15 3.5%), in a weight ratio of 92.5:2.5:5 in N-methyl-2-pyrrolidone was pasted onto an Al foil and dried at 110 °C for 6 h in a vacuum oven. Afterwards, the coated foil was punched into circular pieces with a diameter of 12 mm and the corresponding active material loading was around 11 mg. CR2032 coin-type half cells consisting of an as prepared cathode, a Li metal anode, a Celgard 2325 separator, and 1 M LiPF6 in EC/EMC/DEC (1:1:1 by weight) electrolyte solution were assembled in an Ar-filled glovebox. Electrochemical tests of the as-assembled coin cells were conducted using a battery testing system (LANHE CT2001A, Wuhan LAND Electronics Co., P. R. China) at 2.8-4.3 V (or 4.5 V) at different current densities. Cyclic voltammetry (CV) data were collected at a scan rate of 0.1 mV/s on a Princeton PARSTAT 4000 (AMETEK Co. Ltd.) workstation. Electrochemical impedance spectroscopy (EIS) was carried out using Princeton PARSTAT 4000 in a frequency range from 100 kHz to 10 mHz with an ac amplitude of 5 mV.

### *2.3. Materials Characterization*

The chemical composition of the as-prepared $LiNi_{0.8}Co_{0.1}Mn_{0.1}O_2$ materials was determined using inductively coupled plasma-atomic emission spectrometry (ICP-OES). The morphology and crystallographic structure were measured by scanning electron microscopy (SEM, FEG250, FEI QUANTA), X-ray diffraction (XRD, ADVANCE D8, Bruker), and transmission electron microscopy (TEM, JEM-2100F, JEOL). Rietveld refinement of the XRD data were accomplished by General Structure Analysis System (GSAS) software. The samples analysed by scanning TEM (STEM) were sliced and thinned using a focused ion beam. All XPS spectra were calibrated using the C 1s peak with a binding energy of 284.8 eV. Background subtraction and curve fitting were fulfilled using XPSPEAK Version 4.0 software.

## **3. RESULTS AND DISCUSSION**

As shown in Table 1, ICP-OES is applied to analyse the chemical composition of both A811 and S811. The chemical formulas calculated from the ICP-OES results show the corresponding chemical composition of A811 and S811 materials to be $Li_{1.038}Ni_{0.804}Co_{0.097}Mn_{0.099}O_{2+\delta}$ and $Li_{1.037}Ni_{0.799}Co_{0.097}Mn_{0.099}O_{2+\zeta}$, respectively.

Figure 1(A) and (B) show the differences in morphology and particle size of A811 and S811. A811 is composed of agglomerated spheres with primary particles ranging from 200 to 700 nm, while the primary particles in S811 are of 1-4 um. HRTEM images with the corresponding FFT patterns (inset) in Figure 1(C) and (D) further determine the structure details. For both samples, the HRTEM images and the FFT patterns of the bulk areas exhibit typical structure of $R\overline{3}m$, which are corresponding to the (003) reflections of the layered structure.[21,22]

**Table 1.** The chemical composition results of A811 and S811.

| **Sample** | **Chemical Composition (%)** | | | |
|---|---|---|---|---|
| | **Li** | **Ni** | **Co** | **Mn** |
| A811 | 7.19 | 47.06 | 5.72 | 5.42 |
| S811 | 7.16 | 46.96 | 5.68 | 5.41 |

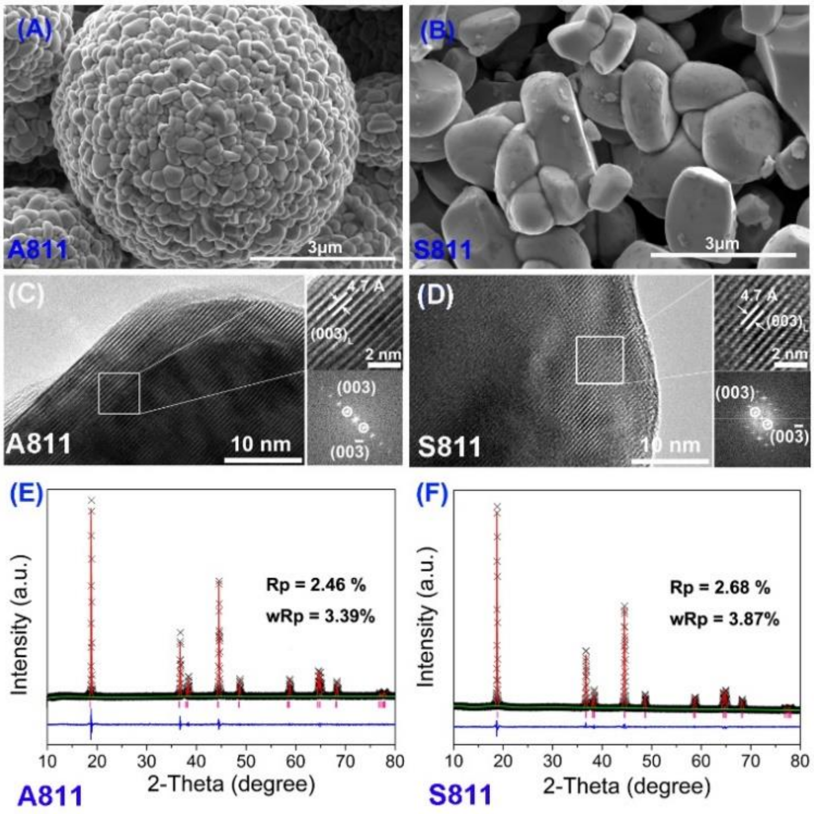

**Figure 1.** SEM images of (A) A811 and (B) S811; HRTEM images with partial enlargements and FFT patterns (inset) of (C) A811 and (D) S811; Reitveld refinement of the XRD patterns for (E) A811 and (F) S811.

XRD patterns of both materials can be indexed to a layered α-$NaFeO_2$ structure with $R\bar{3}m$ symmetry. No extra diffraction peaks are observed in the S811 material as well as A811, suggesting no impurity in the S811 obtained by using higher heating temperature and two-step calcination with additional amount of LiOH

Rietveld refinement of the XRD patterns (Figure 1 (E) and (F)) were carried out to understand the crystallographic parameters differences. Table 2 shows that the Li/Ni cation mixture degree of S811 is higher than that of A811, implying that the different such preparation process of S811 doesn't reduce $Ni^{3+}$ as well as the exchange of transition metals on the 3b sites (transition metal layer) and oxygen on the 6c sites.[23] However, the calculated cell parameters show that S811 has a larger value of a and c axis, which has been reported to benefit the continuous lithium intercalation/deintercalation process.[24]

**Table 2.** Refined crystallographic parameters for A811 and S811.

| Sample | a (Å) | c (Å) | V (Å$^3$) | $I_{(003)}/I_{(104)}$ | $Ni^{2+}$ in Li Layer (%) |
|---|---|---|---|---|---|
| **A811** | 2.8662 | 14.2168 | 101.1423 | 1.285 | 3.96 |
| **S811** | 2.8755 | 14.2122 | 101.7653 | 1.262 | 4.13 |

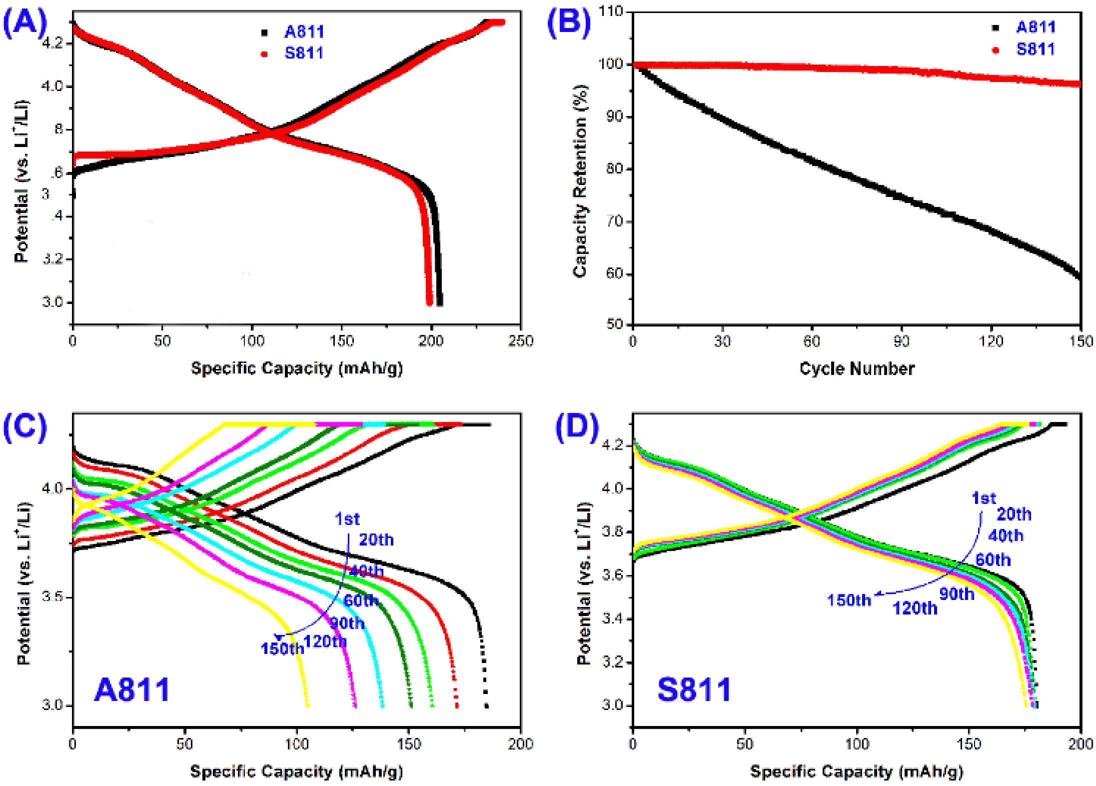

**Figure 2.** (A) The charge/discharge curves of A811 and S811 under condition of 3.0-4.3V @ 0.1C; (B) Cycling performance of A811 and S811 materials cycled between 3.0-4.3 V; Charge-discharge profiles for (C) A811 and (D) S811 at a current density of 200mAh /g (1C ,2nd, 20th, 40th, 60th, 90th, 120th and 150th cycles).

Figure 2(A) exhibits the initial charge/discharge curves of samples at 0.1 C (20 mAh /g) between 3.0-4.3V (vs $Li^+$ /Li) for A811 and S811. The specific capacities of S811 and A811 at 0.1C between 3.0-4.3V are 198.9 mAh /g and 204.7 mAh /g, respectively. The cycling performances of A811 and S811 at a current density of 200mAh /g are shown in Figure 2(B). A811 exhibits a initial capacity of 184.9 mAh /g with the low capacity retention ratio (59.4%) after 150 cycles, while S811 presents initial capacity of 180.5 mAh /g and a high capacity retention of 96.2%. Furthermore, the charge-discharge voltage profiles of A811 and S811 are compared in Figure 2(C) and (D). As is shown, S811 displays significantly improvement on the basis of A811: 1) a greatly enhanced capacity retention, 2) a much slighter voltage decay, 3) a better relieved polarization caused by side reaction during cycling. The superior cycling stability of S811 is reasonable to the related structural improvement originated from a two-step calcination treatment at higher temperature and additional lithium to compensate for Li$^+$ defect caused by lithium volatilization. It can be inferred that such prepared NCM811 material has a stable host structure and suffers little surface invasion or undesired phase transition reaction.

Figure 3(A) and (B) displays the normalized charge-discharge curves of A811 and S811, respectively. There are short plateaus around 4.25V in both curves of A811 and S811 which can be attributed to the typical characteristics of H2→H3 phase transition reaction. However the plateau of A811 is clearer than that of S811. When the upper cut-off voltage is set to be 4.5V, the specific capacity of A811 around 4.25V become even bigger than that of S811. The charge–discharge process for A811 and S811 reveals that the chemical reaction mechanism for each material are similar, involving several phase transitions. H2→H3 phase transition for S811 around 4.25V is compressed to a lower degree other than A811. Such reaction promote the activation of host structure for more Li-ion intercalation/deintercalation, leading to the higher specific capacity of A811. Moreover, as the upper cut-off voltage decreasing to 4.5V, the 1st columbic efficiency of A811 and S811 become close, signifying that the activated host structure of S811 is reversibly utilized more sufficiently than that of A811.

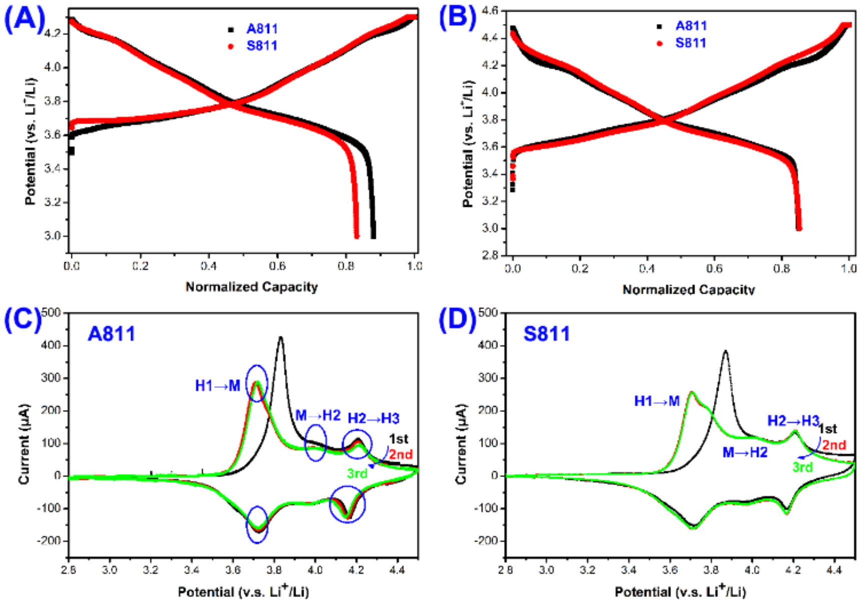

**Figure 3.** Normalized charge/discharge curves of A811 and S811 under different conditions: (A) 3.0-4.3V @ 0.1C; (B) 3.0-4.5V @ 0.1C (1C = 200 mAh /g); CV curves of materials with a scan rate of 0.1 mV/s between 2.8 and 4.5V: (C) A811; (D) S811

Figure 3(C) and (D) shows the CV curves of A811 and S811 at a scanning rate of 0.1 mV/s between 2.8 and 4.5 V. It is appeared that three couples of peaks in both A811 and S811, considered to be related to the oxidation of Ni$^{2+}$ /Ni$^{4+}$, Ni$^{3+}$ /Ni$^{4+}$and Co$^{3+}$ /Co$^{4+}$. For one thing, the integral area of

H2→H3 of A811 is bigger than that of S811， which is in accordance with the charge-discharge curve, certifying that the phase transition is effectively compressed. For another, the CV curves of S811 during three cycles are well overlapped, while A811 shows visible shift or shrinkage in peak or area, especially in the region of H2→H3 peaks. In general, the CV curves suggest that S811 is beneficial to restrict unpleasant phase transition reaction (H2→H3) in a low degree and reduce the electrochemical polarization so that the cathode material stays stable during electrochemical cycles.

In order to understand the origin of the superiority of their electrochemical performance, electrochemical impedance spectra (EIS) of S811 and A811, these samples were measured at open circuit voltage after cell fabrication and 100% SOC after 10th, 50th and 100th cycle. As shown in Figure 4(A), both curves of A811 and S811 at open circuit voltage consist of typically semicircles in high-frequency region and lines in low-frequency region. For those cycled samples at 100% SOC in Figure 4(B), (C) and (D), there are two semicircles and one straight line in each plot. The semicircle in the high frequency region represents the surface film impedance ($R_{sf}$), a semicircle located in the high to medium frequency region represents the charge transfer impedance ($R_{ct}$) and an oblique line located in the low frequency region represents the Warburg impedance ($W_0$).[25]

The Z-view software was used to fit the tested results, and thus-obtained $R_e$, $R_{sf}$ and $R_{ct}$ values of both samples are displayed in Table 3. In the early stages, $R_e$, $R_{sf}$ and $R_{ct}$ values for A811 are smaller than that of S811, which can be reasonably ascribed to larger polarization ofS811 with the big primary particle size. as charge-discharge cycling continue, $R_{sf}$ and $R_{ct}$ for both A811 and S811 increase a lot, but the degree of impedance growth for S811 is much slighter. Such suppression should be attributed to stabler structure of single crystal NCM811 and less side reaction at the out-layer area. It implies that undesired side reaction on S811 is alleviated, signifying slighter SEI interface deposition and charge transfer resistance increase.

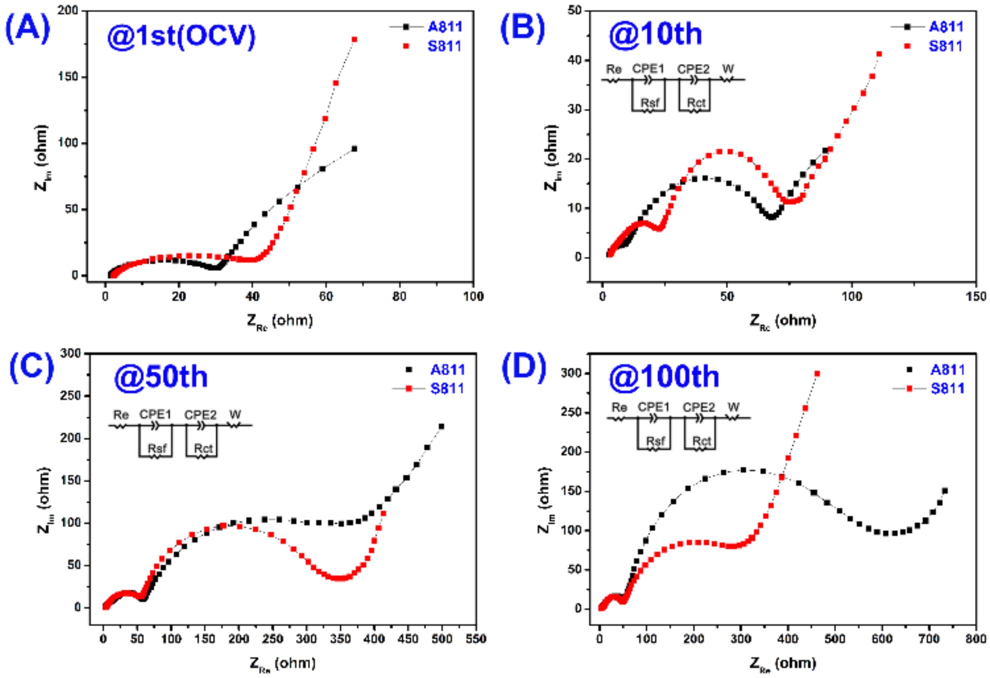

**Figure 4.** Nyquist plots of A811 and S811 during cycling: (A) 1st, (B) 10th, (C) 50th and (D) 100th.

**Table 3.** Fitted results of the EIS for A811 and S811 at 100% SOC

| Sample | Cycle | $R_e$ (Ω) | $R_{sf}$ (Ω) | $R_{ct}$ (Ω) |
|---|---|---|---|---|
| A811 | 10th | 2.5 | 8.9 | 53.5 |
| | 50th | 3.2 | 57.1 | 425.7 |
| | 100th | 3.4 | 74.5 | 496.2 |
| S811 | 10th | 3.4 | 23.7 | 54.6 |
| | 50th | 3.7 | 61.3 | 261.2 |
| | 100th | 3.8 | 62.1 | 316.7 |

The chemical composition and elements condition in the surface of A811 and S811 were analysed by XPS ulteriorly. The raw results and spectra fitted by XPSPEAK software are shown in Figure 5. The survey spectra of both samples suggest that the chemical state of the surface elements of A811 and S811 are similar. Comparing A811 with S811 in Figure 5 (B), there are no shift for the Co 2p and Mn 2p peaks while differences of Ni peaks appear in Ni $2p_{3/2}$ between A811 and S811. By looking into the fitted Ni 2p spectra of A811 and S811, the obvious transferring to higher energy suggests a rise in S811 of valence of the transition metal nickel and covalence of nickel-oxygen other than A811. $Ni^{2+}$ content on the surface of S811 is much higher than that of A811.

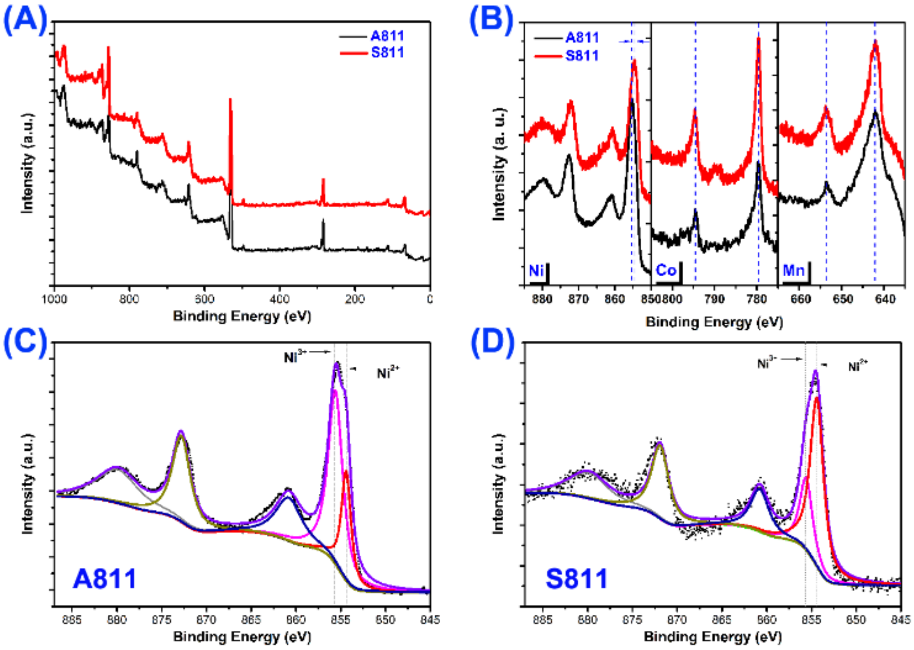

**Figure 5.** XPS spectra and fitting results: (A) original XPS survey spectra for A811 and S811; (B) Ni 2p spectra, Co 2p spectra , Mn 2p spectra for A811 and S811; (C) Ni fitting spectra of A811; (D) Ni fitting spectra of S811.

Such difference on Ni valence state has been demonstrated to be ascribed to the Ni segregation due to the migration ratio difference of transition metals during high temperature heating/tempering process.[26,27] As it has been reported that higher content of $Ni^{2+}$ plays an important role in stabilizing the structure of NCM811 cathode material by pillaring layered structure and reducing local cation mixture. Hence, the better stability of single crystal NCM811 is reasonably attributed more $Ni^{2+}$ ions on the surface.[28]

For the further study on cycling stability difference of A811 and S811, the cross-sectioned SEM image of A811 and S811 are displayed in Figure 6. A811 is composed of primary particles with pores between the grown primary particles; On the other hand, A811 consists of only single crystal with micron scale size . Additionally, after 100 cycles at 1C, the crack and disconnection in A811 grow severely, while S811 displays almost no fracture. Such difference in cracks growth between A811 and S811 can be a further evidence for the better structure stability of single crystal grain than the traditional agglomerated type.[29]

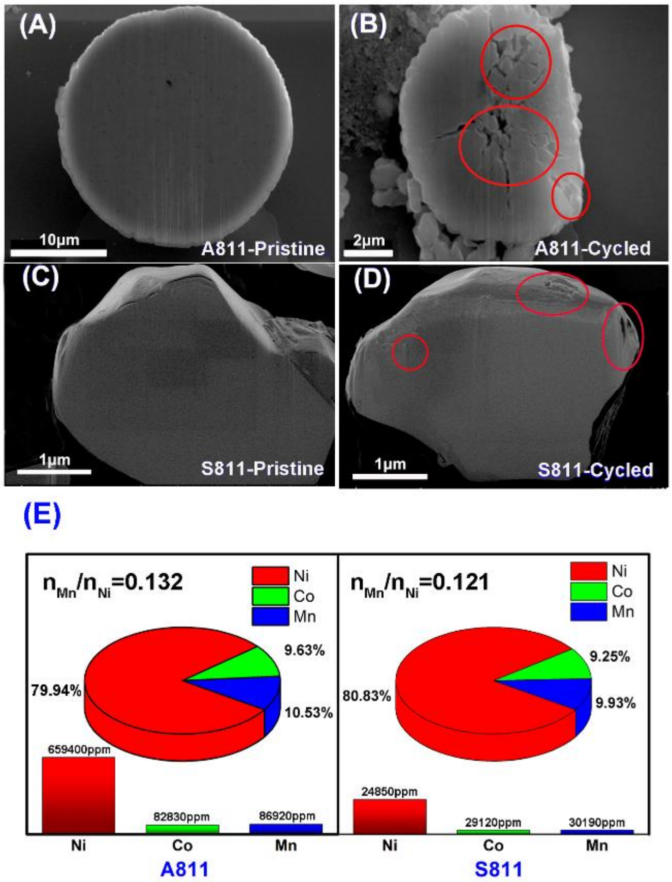

**Figure 6.** SEM images of cross-sectioned A811 and S811 particles: (A) A811 without cycling treatment; (B) A811 after 100 cycles at 1C, 3.0-4.3V; (C) S811 without cycling treatment; (D) S811 after 100 cycles at 1C, 3.0-4.3V; (E) concentrations and proportional relationship of Ni, Co and Mn dissolved in electrolyte

Based on the fact of TM dissolution under high voltage charge process, the concentrations of Ni, Co and Mn dissolved in electrolyte were investigated. For the electrolyte samples with dissolved TM preparation process, both NCM811 materials are galvanostatically charge-discharged for 100 cycles at

1C between 3.0-4.3V. Then the dissolved Ni/Co/Mn of A811 and S811 in the electrolyte are measured by ICP-OES. From the date of dissolved TM element in electrolyte in Figure 6(E), it can be concluded that A811 suffers much severer side reaction or phase transition reaction than S811. What's more, the ratio of dissolved Mn/Ni reveals obvious difference in A811 and S811 samples, which implies severer lopsided Mn loss in A811. Since it is demonstrated that $Mn^{4+}$ other than $Mn^{3+}$ plays an important role in stabilizing the structure of NCM cathode material. Such an lopsided Mn loss should be attributed to the higher $Ni^{2+}$ content in the outlayer area than that of A811. It is reasonable to deduce the higher content of $Ni^{2+}$ at outlayer area is helpful for the formation of a better structured NCM811. Better still, such structure with higher content of $Ni^{2+}$ reduce the exitance of unwelcome $Mn^{3+}$, which causes structure failure such as Jahn-Teller effect.[30]

## 4. CONCLUSION

Ni-Rich NCM cathode material with micron scale grain size is synthesized through two-step sintering at higher temperature with additional LiOH as reactant as well as flux agent. By such preparation approach, specific capacity gap of S811 with A811 of general agglomerated type is greatly reduced. Additionally, it is demonstrated that single crystal NCM811 displays much better electrochemical stability than the traditional agglomerated type NCM811 cathode. It is confirmed that the superiority is related to the fully grown grain size and hence reduced phase transition reaction. As obtained S811 has a much smaller ratio of $Ni^{3+}$ at the surface area, which is beneficial to suppress the undesired side reaction with electrolyte as well as to restrain the crack growth and disconnection.

ACKNOWLEDGEMENTS
The authors would like to acknowledge Zhuzhou ShengHua technology Co. Ltd for financial support, and the National Natural Science Foundation of China (51971250), the National Key Research and Development Program of China (Grant No. 2018YFB010400), the State Key Laboratory of Powder Metallurgy at Central South University.

## References

1. S. F. Tie and C. W. Tan, *Renew. Sust. Energ. Rev.*, 20 **(**2013) 82.
2. M. Li, J. Lu, Z. Chen and K. Amine, *Adv. Mater.*, 30 (2018) 1800561..
3. M. Dubarry, G. Baure, C. Pastor-Fernández, T. F. Yu, W. D. Widanage and J. Marco, *J. Energy Storage*, 21 (2019) 172.
4. J. Lee, A. Urban, X. Li, D. Su, G. Hautier and G. Ceder, *science*, 343 (2014) 519.
5. M. M. Thackeray, S.-H. Kang, C. S. Johnson, J. T. Vaughey, R. Benedek and S. Hackney, *J. Mater. Chem.*, 17 (2007) 3112.
6. H. H. Ryu, K. J. Park, D. R. Yoon, A. Aishova, C. S. Yoon and Y. K. Sun, *Adv. Energy Mater.*, 9 (2019) 1902698.
7. T. Chen, X. Li, H. Wang, X. Yan, L. Wang, B. Deng, W. Ge and M. Qu, *J. Power Sources*, 374 (2018) 1.
8. M. Jo, M. Noh, P. Oh, Y. Kim and J. Cho, *Adv. Energy Mater.*, 4 (2014) 1301583.

9. J.-M. Lim, T. Hwang, D. Kim, M.-S. Park, K. Cho and M. Cho, *Sci. Rep.*, 7 (2017) 39669.
10. Liang, R. C. Longo, F. Kong, C. Zhang, Y. Nie, Y. Zheng and K. Cho, *ACS Appl. Mater. Inter.*, 10 (2018)
11. 6673.
12. S. Gao, X. Zhan and Y.-T. Cheng, *J. Power Sources*, 410 (2019) 45.
13. L. Zhou, K. Zhang, Z. Hu, Z. Tao, L. Mai, Y.-M. Kang, S.-L. Chou and J. Chen, *Adv. Energy Mater.*, 8 (2018) 1701415.
14. J. Li, W. Li, Y. You and A. Manthiram, *Adv. Energy Mater.*, 8 (2018) 1801957.
15. X. Han, Q. Meng, T. Sun and J. Sun, *J. Power Sources*, 195 (2010) 3047.
16. Z.-D. Huang, X.-M. Liu, S.-W. Oh, B. Zhang, P.-C. Ma and J.-K. Kim, *J. Mater. Chem.*, 21(2011) 10777.
17. L. Wang, B. Wu, D. Mu, X. Liu, Y. Peng, H. Xu, Q. Liu, L. Gai and F. Wu, *J. Alloy. Compd.*, 674 (2016) 360.
18. X. Xu, H. Huo, J. Jian, L. Wang, H. Zhu, S. Xu, X. He, G. Yin, C. Du and X. Sun, *Adv. Energy Mater.*, 9 (2019) 1803963.
19. J.-x. WANG, X.-h. LI, Z.-x. WANG, L.-j. LI, H.-j. GUO, Y. Peng and W. Ling, *The Chinese Journal of Nonferrous Metals*, 21 (2011) 2175.
20. Y. Huang, Z.-x. Wang, X.-h. Li, H.-j. Guo and J.-x. Wang, *T. Nonferr. Metal. Soc.*, 25 (2015) 2253.
21. M.-H. Kim, H.-S. Shin, D. Shin and Y.-K. Sun, *J. Power Sources*, 159(2006) 1328.
22. K.-J. Park, H.-G. Jung, L.-Y. Kuo, P. Kaghazchi, C. S. Yoon and Y.-K. Sun, *Adv. Energy Mater.*, 8 (2018) 1801202.
23. B. Han, S. Xu, S. Zhao, G. Lin, Y. Feng, L. Chen, D. G. Ivey, P. Wang and W. Wei, *ACS Appl. Mater. Interfaces*, 10 (2018) 39599.
24. K. Park, J.-H. Park, S.-G. Hong, B. Choi, S. Heo, S.-W. Seo, K. Min and J.-H. Park, *Sci. Rep.*, 7 (2017) 44557.
25. F. Kong, C. Liang, R. C. Longo, D.-H. Yeon, Y. Zheng, J.-H. Park, S.-G. Doo and K. Cho, *Chemistry of Materials*, 28 (2016) 6942.
26. T. Kim, L. K. Ono, N. Fleck, S. R. Raga and Y. Qi, *J. Mater. Chem. A.*, 6 (2018) 14449.
27. P. Yan, J. Zheng, J. Zheng, Z. Wang, G. Teng, S. Kuppan, J. Xiao, G. Chen, F. Pan and J. G. Zhang, *Adv. Energy Mater.*, 6 (2016) 1502455.
28. F. Lin, D. Nordlund, Y. Li, M. K. Quan, L. Cheng, T.-C. Weng, Y. Liu, H. L. Xin and M. M. Doeff, *Nat. Energy*, 1 (2016) 15004.
29. K. Meng, Z. Wang, H. Guo, X. Li and D. Wang, *Electrochim. Acta*, 211 (2016) 822.
30. P. Yan, J. Zheng, T. Chen, L. Luo, Y. Jiang, K. Wang, M. Sui, J.-G. Zhang, S. Zhang and C. Wang, *Nat. Comm.*, 9 (2018) 2437.
31. S. Gao, X. Zhan and Y.-T. Cheng, *J. Power Sources*, 410 (2019) 45.